

Tunable Single-Photon Transport in a Multi-mode Waveguide via a Λ -Type Emitter

Yan Liu,¹ Qing-Ao Xiang,¹ Xin-Yuan Yang,¹ Ji-Bing Yuan,¹ Shi-Qing Tang,¹ Xin-Wen Wang,¹ and Ya-Ju Song^{1,*}

¹*Key Laboratory of Opto-electronic Control and Detection Technology of University of Hunan Province,
and College of Physics and Electronic Engineering,
Hengyang Normal University, Hengyang 421002, China*

(Dated: December 1, 2025)

Precise control of photon transport in waveguide quantum electrodynamics is fundamental to advancing quantum information processing. We investigate the manipulation of single-photon scattering via a driven Λ -type emitter coupled to a rectangular waveguide, examining both single- and multi-mode regimes. Using the Lippmann-Schwinger formalism, we derive the scattering matrix and identify two distinct control mechanisms: Fano resonances induce complete reflection, and electromagnetically induced transparency (EIT) induce perfect transmission. In the single-mode regime, the external drive parameters—the detuning and Rabi frequency—precisely tune the positions and number of reflection peaks, allowing dynamic spectral engineering. In the multi-mode regime, quantum interference between modes governs the scattering dynamics. When the input photon is prepared in a specific coherent superposition, multi-mode effects restore single-mode-like behavior, enabling Fano-mediated complete reflection. Conversely, a single-mode input prevents complete reflection even at the Fano resonance, while EIT-driven transmission persists. These results demonstrate a versatile toolbox for photonic quantum control in multi-mode waveguides, paving the way for applications such as broadband dual-frequency filters and multi-mode spectrometers.

I. INTRODUCTION

Waveguide quantum electrodynamics (waveguide QED) delves into the interaction between photons and quantum emitters, such as atoms, quantum dots, or superconducting qubits, within a photonic continuum [1–5]. In comparison to cavity QED, waveguide QED exhibits remarkable scalability, integrability, and bandwidth, rendering it a crucial resource for quantum communication [6–9], quantum computing [10], and quantum simulation [11]. All of these applications demand precise control over photon transport to realize essential functionalities such as high-fidelity quantum gates, efficient state transfer, and scalable quantum networks. Currently, a variety of control strategies are employed to achieve this precision, leveraging phenomena such as electromagnetically induced transparency (EIT), Fano resonances, collective emission, and quantum interference. For instance, EIT creates a narrow transparency window through coherent driving [12], while Fano resonances yield perfect reflection at specific frequencies via destructive interference between a discrete state and a continuum [13, 14]. This framework has been enriched by non-Hermitian physics, where engineered exceptional points enable exotic few-photon bound states [15]. More recently, the field is expanding beyond these paradigms with emerging approaches like giant atom systems [16–20], topological waveguides [21, 22], and non-perturbative theories [23].

In the field of waveguide QED, research has primarily focused on the interaction between photons and quantum emitters within idealized one-dimensional waveguide systems [24–26]. In such waveguides, photons are confined

to a single fundamental spatial mode. Then the photon-emitter interaction can be effectively treated as a one-dimensional problem, a simplification often enabled by the Wigner-Weisskopf approximation. However, the operational bandwidth of ideal one-dimensional waveguides is inherently limited, which also constrains the performance of related quantum devices, such as single-photon switches and quantum routers.

Practical waveguide implementations—including dielectric waveguides on integrated photonic chips and hollow-core photonic crystal fibers used in cold-atom experiments—feature finite transverse cross-sections [27]. The advent of high-frequency light sources, such as X-rays and free-electron lasers [28–30], has further motivated the study of waveguides with cross-sectional dimensions far exceeding the wavelengths. These systems can simultaneously support multiple transverse electric (TE) and transverse magnetic (TM) propagating modes [31–35], thereby opening a complex frontier in multi-mode waveguide QED. In this regime, the ability to utilize these additional modes enhances the information capacity of photonic systems. For instance, multi-mode interactions can facilitate nonlinear optical processes like four-wave mixing and parametric amplification. More importantly, they provide a platform for generating high-dimensional quantum states, such as mode-entangled states, which are essential for high-dimensional quantum multiplexing and information processing [36]. However, the photon scattering in such multi-mode environments is a complex multi-channel process. The quantum emitter acts as a coupler between different waveguide modes, leading to intricate multi-path quantum interference that can drastically alter the single-photon transport properties. Theoretical mechanisms that are highly effective in single-mode systems, such as Fano resonance, are often suppressed in multi-mode structures due to the presence

* yjsong@hynu.edu.cn

of competing scattering channels [14, 35]. Consequently, the development of new theoretical frameworks that accurately account for the multi-mode structure is essential for achieving precise control over single-photon states and harnessing the potential of multi-mode waveguides for quantum information applications.

In this paper, we theoretically investigate single-photon scattering in a rectangular waveguide coupled to a driven Λ -type quantum emitter. One transition of the Λ -emitter is directly coupled to the waveguide, while an external field drives the second, converting the Λ system into an effective V-type emitter whose two transition frequencies and coupling strengths are continuously tunable by the drive [37–41]. This tunable three-level emitter acts as a quantum switch, enabling EIT or Fano reflection on demand. Using the Lippmann-Schwinger formalism [42–44], we derive an exact analytical scattering matrix valid for both single-mode and multi-mode regimes. Our analysis reveals rich and controllable scattering phenomena. In the single-mode region, the emitter induces two distinct reflection resonances and an EIT transmission window. In the multi-mode region, we demonstrate that this control mechanism can be extended by exploiting the quantum interference between different transverse modes. Specifically, we derive the exact input-state conditions for complete reflection with a properly engineered superposition of waveguide modes. Our framework furnishes an exact description of multi-mode waveguide QED and underpins the design of broadband dual-frequency filters, mode-selective routers, and other reconfigurable quantum photonic devices, while opening a route to higher-dimensional photonic quantum technologies.

The paper is structured as follows: Section II presents the physical model and derives the multi-mode scattering formalism. Section III establishes analytical conditions for complete transmission and reflection in multi-mode waveguide QED systems, while also investigating driving-field modulation mechanisms within the dressed-state framework. Section IV explores how a driven Λ -type emitter enables precise control over single-photon transport in both single- and multi-mode waveguide regimes. Finally, conclusions are drawn in Section V.

II. PHYSICAL MODEL AND MULTI-MODE SCATTERING FORMALISM

In this section, we first present the physical model and Hamiltonian describing a driven Λ -type emitter coupled to an infinite rectangular waveguide. Subsequently, we derive the exact multi-mode scattering matrix for this waveguide QED system using the Lippmann-Schwinger formalism, obtaining closed-form expressions for the reflection and transmission amplitudes of arbitrary single-photon input states.

A. System Hamiltonian

We consider a driven Λ -type three-level emitter coupled to an infinitely long rectangular waveguide with cross-sectional dimensions $a = 1.5b$ (see Fig. 1). The emitter, located at position $(a/2, b/2, z_0)$, consists of a ground state $|g\rangle$, an intermediate state $|f\rangle$, and an excited state $|e\rangle$, with respective energies ω_g , ω_f , and ω_e . Here, ω_g is set to zero as a reference. The emitter's z -oriented dipole moment selectively interacts with the TM modes. The waveguide supports TM_{mn} modes indexed by $j = 1, 2, 3, \dots$ corresponding to TM_{11} , TM_{31} , TM_{13} , etc., ordered by increasing cutoff frequencies $\omega_j = \pi\sqrt{m^2/a^2 + n^2/b^2}$ (units $\hbar = c = 1$). Each mode is described by annihilation and creation operators $\hat{a}_{j,k}$, $\hat{a}_{j,k}^\dagger$ for photons of wavevector $\mathbf{k} = (m\pi/a, n\pi/b, k)$. The waveguide obeys the dispersion relation $\omega_{j,k} = \sqrt{\omega_j^2 + k^2}$. The waveguide TM modes mediate the $|e\rangle \leftrightarrow |g\rangle$ transition, whereas a classical field characterized by Rabi frequency Ω and detuning δ coherently drives the $|e\rangle \leftrightarrow |f\rangle$ transition.

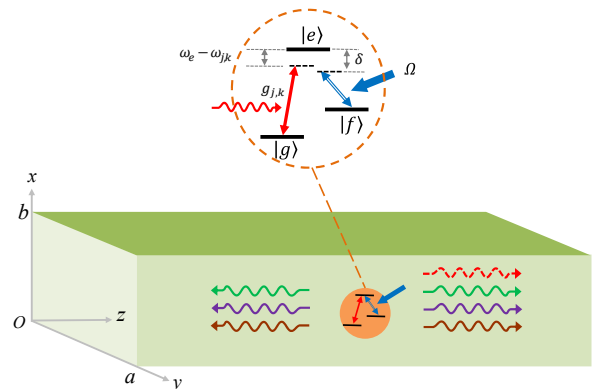


FIG. 1. (color online) Schematic of a driven Λ -type emitter coupled to an infinite rectangular waveguide (cross-section $A = ab, a = 1.5b$). The waveguide couples $|e\rangle \leftrightarrow |g\rangle$ with strength $g_{j,k}$ and detuning $\omega_e - \omega_{j,k}$, while a classical field drives $|e\rangle \leftrightarrow |f\rangle$ with Rabi frequency Ω and detuning δ . The waveguide follows the dispersion $\omega_{j,k} = \sqrt{\omega_j^2 + k^2}$ ($\hbar = c = 1$), supports TM_{mn} modes indexed by TM_j in ascending cutoff order $\omega_j = \pi\sqrt{m^2/a^2 + n^2/b^2}$, and k is the longitudinal wave number.

Within the rotating-wave approximation and in the drive-field rotating frame, the system Hamiltonian $\hat{H} =$

$\hat{H}_0 + \hat{V}$ comprises [14, 31–33]:

$$\hat{H}_0 = \omega_e |e\rangle\langle e| + (\omega_e - \delta) |f\rangle\langle f| + \sum_j \int_{-\infty}^{+\infty} dk \omega_{j,k} \hat{a}_{j,k}^\dagger \hat{a}_{j,k} \quad (1)$$

$$\hat{V} = \sum_j \int_{-\infty}^{+\infty} dk (g_{j,k} |e\rangle\langle g| \hat{a}_{j,k} + g_{j,k}^* |g\rangle\langle e| \hat{a}_{j,k}^\dagger) + \Omega(|e\rangle\langle f| + |f\rangle\langle e|), \quad (2)$$

where the free Hamiltonian \hat{H}_0 describes the uncoupled emitter and waveguide modes, and the interaction Hamiltonian \hat{V} contains both emitter-waveguide coupling and classical field driving. The emitter-waveguide coupling strength is $g_{j,k} = -g\omega_j \sin(\frac{m\pi}{2}) \sin(\frac{n\pi}{2}) e^{-ikz_0} / \sqrt{\omega_{j,k}}$, where $g = \mu_e / \sqrt{\varepsilon\pi A}$ is determined by the dipole matrix element μ_e and the cross-sectional area $A = ab$ [14]. The coupling strength vanishes for modes with even m or n because the emitter sits at the center of the waveguide cross section.

B. Multi-mode Scattering Matrix via the Lippmann-Schwinger equation

To characterize the single-photon scattering, we introduce the scattering matrix S that connects asymptotic input and output states. The system is initialized with the emitter in the ground state $|g\rangle$ and a single photon in the TM_j waveguide mode $|\varphi_{j,k}\rangle = \hat{a}_{j,k}^\dagger |0\rangle$, where $|0\rangle$ denotes the photonic vacuum and k the longitudinal wave number. The input state $|\varphi_{j,k}\rangle |g\rangle$ is an eigenstate of the free Hamiltonian \hat{H}_0 with energy $\omega = \omega_{j,k}$, whereas the scattering state $|\varphi_{j,k}^{(+)}\rangle$ is an eigenstate of the total Hamiltonian $\hat{H} = \hat{H}_0 + \hat{V}$ at the same energy and satisfies the Lippmann-Schwinger equation [43]

$$|\varphi_{j,k}^{(+)}\rangle = |\varphi_{j,k}\rangle |g\rangle + \frac{1}{\omega - \hat{H}_0 + i0^+} \hat{V} |\varphi_{j,k}^{(+)}\rangle. \quad (3)$$

Excitation-number conservation restricts the single-excitation scattering state to the form

$$|\varphi_{j,k}^{(+)}\rangle = \sum_{j'} \int_{-\infty}^{+\infty} dk' u_{j',k';j,k} |\varphi_{j',k'}\rangle |g\rangle + \alpha_{j,k} |0\rangle |e\rangle + \beta_{j,k} |0\rangle |f\rangle, \quad (4)$$

where $u_{j',k';j,k}$ is the probability amplitude for photon emission into the $TM_{j'}$ mode with longitudinal wave number k' , while $\alpha_{j,k}$ and $\beta_{j,k}$ denote the emitter excitation amplitudes to $|e\rangle$ and $|f\rangle$, respectively. Substituting

Eq. (4) into Eq. (3) yields

$$\alpha_{j,k} = \frac{\sum_{j'} \int dk' g_{j',k'} u_{j',k';j,k} + \Omega \beta_{j,k}}{\omega - \omega_e + i0^+}, \quad (5a)$$

$$\beta_{j,k} = \frac{\Omega \alpha_{j,k}}{\omega - \omega_e + \delta + i0^+}, \quad (5b)$$

$$u_{j',k';j,k} = \frac{\alpha_{j,k} g_{j',k'}^*}{\omega - \omega_{j',k'} + i0^+} + \delta_{j',j} \delta_{k,k'}. \quad (5c)$$

Solving Eqs. (5a)-(5c) yields the excited-state amplitude

$$\alpha_{j,k} = \frac{g_{j,k}}{\omega - \omega_e - \frac{\Omega^2}{\omega - \omega_e + \delta} - \Delta(\omega) + i\Gamma(\omega)}. \quad (6)$$

During the calculation we used the Sokhotski-Plemelj identity $\lim_{\varepsilon \rightarrow 0^+} (x - x_0 + i\varepsilon)^{-1} = \mathcal{P}[(x - x_0)^{-1}] - i\pi\delta(x - x_0)$ (with \mathcal{P} the Cauchy principal value) to decompose the self-energy $\Sigma(\omega) = \sum_j \int_{-\infty}^{+\infty} dk |g_{j,k}|^2 / (\omega - \omega_{j,k} + i0^+)$ into the Lamb shift $\Delta(\omega)$ and decay rate $\Gamma(\omega)$,

$$\Delta(\omega) = \sum_j \Delta_j(\omega), \quad (7a)$$

$$\Gamma(\omega) = \sum_j \Gamma_j(\omega). \quad (7b)$$

The mode-resolved contributions are defined by

$$\Delta_j(\omega) = \mathcal{P} \int_{-\infty}^{+\infty} dk \frac{|g_{j,k}|^2}{\omega - \omega_{j,k}}, \quad (8a)$$

$$\Gamma_j(\omega) = 2\pi |g_{j,k_j}|^2 \rho_j(\omega), \quad (8b)$$

where the density of states is derived from the dispersion relation,

$$\rho_j = \left| \frac{1}{d\omega/dk|_{k=\pm k_j}} \right| = \frac{\omega}{\sqrt{\omega^2 - \omega_j^2}} \Theta(\omega - \omega_j), \quad (9)$$

with $k_j = \sqrt{\omega^2 - \omega_j^2}$ and $\Theta(\omega - \omega_j)$ the Heaviside step function.

With the interaction Hamiltonian \hat{V} from Eq. (2) and the scattering state from Eq. (4), the on-shell T matrix element is [43]

$$T_{j'k' \leftarrow jk} = \langle g | \langle \varphi_{j',k'} | \hat{V} | \varphi_{j,k}^{(+)} \rangle = \alpha_{j,k} g_{j',k'}^*. \quad (10)$$

Then the scattering operator \hat{S} follows by inserting Eqs. (6) and (10) into $S_{j'k' \leftarrow jk} = \delta_{j,j'} \delta_{k,k'} - 2\pi i \delta(\omega_{j',k'} - \omega) T_{j'k' \leftarrow jk}$, resulting in

$$S_{j'k' \leftarrow jk} = \delta_{j,j'} \delta_{k,k'} - \frac{2\pi i g_{j,k} g_{j',k'}^*}{G(\omega)} \delta(\omega_{j',k'} - \omega), \quad (11)$$

where the function $G(\omega)$ is defined as

$$G(\omega) = \omega - \omega_e - \frac{\Omega^2}{\omega - \omega_e + \delta} - \Delta(\omega) + i\Gamma(\omega). \quad (12)$$

Equation (11) describes the single-photon scattering dynamics, where the first term corresponds to direct transmission and the second term represents the emitter-mediated scattering. An incident photon in the k -th TM _{j} mode couples to the emitter with strength $g_{j,k}$, driving $|g\rangle \rightarrow |e\rangle$. Subsequent decay back to $|g\rangle$ allows re-emission into either the original k -th TM _{j} mode or any other k' -th TM _{j'} mode via $g_{j',k'}$. The scattering exhibits two key characteristics. Firstly, the classical drive operating between states $|e\rangle$ and $|f\rangle$ exerts a modulating influence on the scattering process through the function $G(\omega)$ in Eq. (12). Furthermore, the external field facilitates the on-demand and controlled interconversion among various guided TM modes with the strict adherence to energy conservation, denoted by $\delta(\omega_{j',k'} - \omega)$.

C. General expressions for reflection and transmission amplitudes

With the emitter initially in the ground state $|g\rangle$ and an incident photon at frequency ω , the input state can be expressed as a superposition over all accessible modes:

$$|\varphi_{\text{in}}\rangle = \sum_{j=1}^{j_{\text{max}}} c_j |\varphi_{j,k_j}\rangle, \quad (13)$$

where c_j are normalized amplitudes, and the longitudinal wave number for the j -th mode is given by $k_j = \sqrt{\omega^2 - \omega_j^2}$. The total number of participating modes, j_{max} , is determined by the relative magnitudes of the input-photon frequency and the cutoff frequencies, satisfying $\omega_{j_{\text{max}}} < \omega < \omega_{j_{\text{max}}+1}$. While single-mode operation is confined to the regime $\omega_1 < \omega < \omega_2$ ($j_{\text{max}} = 1$), practical waveguides support multiple TM modes once $\omega > \omega_2$ ($j_{\text{max}} > 1$).

The outgoing state is derived from the multi-mode S -matrix presented in Eq. (11):

$$\begin{aligned} |\varphi_{\text{out}}\rangle &= \hat{S}|\varphi_{\text{in}}\rangle = \sum_{j'=1}^{j_{\text{max}}} \sum_{j=1}^{j_{\text{max}}} \int dk' c_j S_{j'k' \leftarrow jk_j} |\varphi_{j',k'}\rangle \\ &= \sum_{j=1}^{j_{\text{max}}} t_j |\varphi_{j,k_j}\rangle + r_j |\varphi_{j,-k_j}\rangle. \end{aligned} \quad (14)$$

Here, the reflection and transmission amplitudes are defined as

$$r_j = \frac{-2\pi i \rho_j(\omega) g_{j,-k_j}^*}{G(\omega)} \sum_{j=1}^{j_{\text{max}}} c_j g_{j,k_j}, \quad (15a)$$

$$t_j = c_j - \frac{2\pi i \rho_j(\omega) g_{j,k_j}^*}{G(\omega)} \sum_{j=1}^{j_{\text{max}}} c_j g_{j,k_j}. \quad (15b)$$

The function $G(\omega)$ is specified in Eq. (12), with $\Delta(\omega) = \sum_{j=1}^{j_{\text{max}}} \Delta_j(\omega)$ and $\Gamma(\omega) = \sum_{j=1}^{j_{\text{max}}} \Gamma_j(\omega)$ as derived from

Eqs. (7a)-(8b). The reflectance and transmittance in the j -th scattering channel are subsequently obtained from the scattering amplitudes and the group velocities $|v_{g,j}| = |d\omega/dk|_{k=k_j} = \rho_j^{-1}$ given by Eq. (9) as

$$R_j = \frac{|r_j|^2 \rho_j^{-1}(\omega)}{\sum_{j=1}^{j_{\text{max}}} |c_j|^2 \rho_j^{-1}(\omega)}, \quad (16a)$$

$$T_j = \frac{|t_j|^2 \rho_j^{-1}(\omega)}{\sum_{j=1}^{j_{\text{max}}} |c_j|^2 \rho_j^{-1}(\omega)}. \quad (16b)$$

Thus the total reflectance $R = \sum_{j=1}^{j_{\text{max}}} R_j$ and total transmittance $T = \sum_{j=1}^{j_{\text{max}}} T_j$ are

$$R = 1 - T = \frac{2\pi\Gamma(\omega) \left| \sum_{j=1}^{j_{\text{max}}} c_j g_{j,k_j} \right|^2}{|G(\omega)|^2 \sum_{j=1}^{j_{\text{max}}} |c_j|^2 \rho_j^{-1}(\omega)}. \quad (17)$$

III. PERFECT SCATTERING CONTROL VIA THE DRIVING FIELD IN MULTI-MODE WAVEGUIDE QED

This section establishes analytical criteria for complete transmission and reflection in the multi-mode waveguide QED systems. Building on the scattering framework of Sec. II, we employ the dressed-states formalism to explain how Fano resonance induces complete reflection and how EIT or dark states accounts for complete transmission. These results offer explicit transport control guidelines across single- and multi-mode regimes, laying the theoretical basis for subsequent input-state-dependent protocols.

By substituting Eqs. (7b), (8b), and (12) into Eq. (17), we derive the following relationship for the total reflectance:

$$\begin{aligned} R &= \frac{2\pi\Gamma(\omega) \left| \sum_{j=1}^{j_{\text{max}}} c_j g_{j,k_j} \right|^2}{\{\text{Re}^2 [G(\omega)] + \Gamma^2(\omega)\} \sum_{j=1}^{j_{\text{max}}} |c_j|^2 \rho_j^{-1}(\omega)} \\ &\leq \frac{\left| \sum_{j=1}^{j_{\text{max}}} c_j g_{j,k_j} \right|^2}{\sum_{j=1}^{j_{\text{max}}} |g_{j,k_j}|^2 \rho_j(\omega) \sum_{j=1}^{j_{\text{max}}} |c_j|^2 \rho_j^{-1}(\omega)} \\ &\leq 1. \end{aligned} \quad (18)$$

Equation (18) reveals two complete transmission mechanisms. First, the dark-state condition ($\sum_{j=1}^{j_{\text{max}}} c_j g_{j,k_j} = 0$) achieves $\hat{V}|\varphi_{\text{in}}\rangle = 0$ and induces destructive interference, thereby enabling complete transparency. Second, the two-photon resonance condition ($\delta = \omega_e - \omega$) causes $|G(\omega)| \rightarrow \infty$, facilitating EIT irrespective of the input state. In the EIT mechanism, there are two excitation paths from $|g\rangle$ to $|e\rangle$: direct waveguide coupling or $|g\rangle \rightarrow |e\rangle \rightarrow |f\rangle \rightarrow |e\rangle$ via the intermediate state $|f\rangle$. The two-photon resonance condition equalizes the amplitudes of these two paths, leading to destructive interference that suppresses the population of $|e\rangle$. Adjusting

TABLE I. Complete transmission (CTPs) and complete reflection peaks (CRPs) conditions under driving field

Detuning Range	CTP Conditions (excluding dark-state cases)	CRP Conditions : $j_{\max} = 1$ or $c_j \propto \rho_j g_{j,k_j}^*$
Outside EIT window $\delta \notin (\omega_e - \omega_{j_{\max}+1}, \omega_e - \omega_{j_{\max}})$	0 CTP	<ul style="list-style-type: none"> • 0 CRPs if $\text{Re}[G(\omega_{j_{\max}})]\text{Re}[G(\omega_{j_{\max}+1})] > 0$ • 1 CRP if $\text{Re}[G(\omega_{j_{\max}})] < 0 < \text{Re}[G(\omega_{j_{\max}+1})]$
Within EIT window $\delta \in (\omega_e - \omega_{j_{\max}+1}, \omega_e - \omega_{j_{\max}})$	1 CTP occurs at $\omega = \omega_e - \delta$	<ul style="list-style-type: none"> • 0 CRPs if $\text{Re}[G(\omega_{j_{\max}})] > 0 > \text{Re}[G(\omega_{j_{\max}+1})]$ • 1 CRP if $\text{Re}[G(\omega_{j_{\max}})]\text{Re}[G(\omega_{j_{\max}+1})] > 0$ • 2 CRPs if $\text{Re}[G(\omega_{j_{\max}})] < 0 < \text{Re}[G(\omega_{j_{\max}+1})]$

$\delta \in (\omega_e - \omega_{j_{\max}+1}, \omega_e - \omega_{j_{\max}})$ allows for complete transmission when $\omega = \omega_e - \delta$, as depicted in the gray-shaded region in Fig. 2(a).

Having elucidated the transmission characteristics, we now shift our focus to the reflection-related phenomena. The first inequality in Eq. (18) holds if and only if the real part of $G(\omega)$ vanishes, satisfying the Fano-resonance condition $\text{Re}[G(\omega)] = \omega - \omega_e - \Omega^2/(\omega - \omega_e + \delta) - \Delta(\omega) = 0$. By the Cauchy-Schwarz inequality, the second inequality attains equality precisely when either the system operates in the single-mode regime ($j_{\max} = 1$), or the photon is prepared in a specific coherent superposition state (SCSS) with $c_j \propto \rho_j g_{j,k_j}^*$ in the multi-mode regime. The Fano resonance condition governs complete-reflection peak (CRP) count. By using the monotonicity of $\text{Re}[G(\omega)]$, we can elucidate how the driving-field parameters Ω and δ precisely control the number of its zeros within the frequency region $\omega \in [\omega_{j_{\max}}, \omega_{j_{\max}+1}]$. For $\delta \notin (\omega_e - \omega_{j_{\max}+1}, \omega_e - \omega_{j_{\max}})$, monotonic increase allows at most one CRP when $\text{Re}[G(\omega_{j_{\max}})] < 0 < \text{Re}[G(\omega_{j_{\max}+1})]$ and none otherwise. For $\delta \in (\omega_e - \omega_{j_{\max}}, \omega_e - \omega_{j_{\max}+1})$, $\text{Re}[G(\omega)]$ increases on both sides of the divergence at $\omega = \omega_e - \delta$, resulting in no CRPs if $\text{Re}[G(\omega_{j_{\max}})] > 0 > \text{Re}[G(\omega_{j_{\max}+1})]$, one CRP if $\text{Re}[G(\omega_{j_{\max}})]\text{Re}[G(\omega_{j_{\max}+1})] > 0$, and two CRPs if $\text{Re}[G(\omega_{j_{\max}})] < 0 < \text{Re}[G(\omega_{j_{\max}+1})]$.

The complete transmission and complete reflection conditions derived above exclude photon frequencies at mode cut-offs (discussed in Sec. IV). Table I summarizes the driving-field dependence: the number of CTPs is set by δ , whereas the number of CRPs is determined by δ together with the sign changes of $\text{Re}[G(\omega_j)]$ across the band (cut-off effects omitted). The unified conditions for $T = 1$ and $R = 1$ in both single- and multi-mode regimes read

$$T = 1 : \sum_{j=1}^{j_{\max}} c_j g_{j,k_j} = 0 \text{ or } \delta = \omega_e - \omega, \quad (19a)$$

$$R = 1 : \text{Re}[G(\omega)] = 0 \text{ and } (j_{\max} = 1 \text{ or } c_j \propto \rho_j g_{j,k_j}^*). \quad (19b)$$

To reveal the physics underlying complete-reflection control, we adopt the dressed-state basis. The classical

drive diagonalizes the $\{|e\rangle, |f\rangle\}$ subspace into

$$|\nu_+\rangle = \sin\theta|e\rangle + \cos\theta|f\rangle, \quad (20a)$$

$$|\nu_-\rangle = -\cos\theta|e\rangle + \sin\theta|f\rangle, \quad (20b)$$

with $\tan\theta = 2\Omega/(\sqrt{4\Omega^2 + \delta^2} - \delta)$ and eigenenergies

$$\nu_{\pm} = \omega_e + \frac{-\delta \pm \sqrt{4\Omega^2 + \delta^2}}{2}. \quad (21)$$

The total Hamiltonian can be rewritten as

$$\begin{aligned} \hat{H} = & \sum_{i=\pm} \nu_i |\nu_i\rangle \langle \nu_i| + \sum_j \int_{-\infty}^{+\infty} dk \omega_{j,k} \hat{a}_{j,k}^\dagger \hat{a}_{j,k} \\ & + \sum_j \int_{-\infty}^{+\infty} dk (\sin\theta g_{j,k} |\nu_+\rangle \langle g| \hat{a}_{j,k} \\ & - \cos\theta g_{j,k} |\nu_-\rangle \langle g| \hat{a}_{j,k} + H.c.). \end{aligned} \quad (22)$$

So the driven Λ -type emitter behaves as an effective V-type emitter whose transitions $|g\rangle \leftrightarrow |\nu_{\pm}\rangle$ couple to the waveguide with tunable strengths $\sin\theta g_{j,k}$ and $-\cos\theta g_{j,k}$, respectively. The complete reflection condition $\text{Re}[G(\omega)] = 0$ reads

$$\begin{aligned} & [\omega - \nu_+ - \sin^2\theta\Delta(\omega)][\omega - \nu_- - \cos^2\theta\Delta(\omega)] \\ & = \sin^2\theta \cos^2\theta \Delta^2(\omega). \end{aligned} \quad (23)$$

In the weak-coupling limit, we drop the second-order Lamb shift term and approximate $\Delta(\omega) \approx \Delta(\omega_e)$, giving the renormalized resonance frequencies

$$\tilde{\nu}_+ = \nu_+ + \sin^2\theta\Delta(\omega_e), \quad (24a)$$

$$\tilde{\nu}_- = \nu_- + \cos^2\theta\Delta(\omega_e). \quad (24b)$$

Figure 2(b) superimposes the exact zeros of $\text{Re}[G(\omega)]$ (solid black curves) and the approximate conditions $\omega = \tilde{\nu}_{\pm}$ (dotted white curves). Their near-perfect overlap confirms that complete reflection occurs whenever the input photon matches the tunable re-normalized transition frequencies $\tilde{\nu}_{\pm}$. This reflection is a Fano resonance: at $\omega = \tilde{\nu}_{\pm}$ the directly transmitted and re-emitted waves acquire a relative phase of π in Eq. (15b), leading to vanishing transmission.

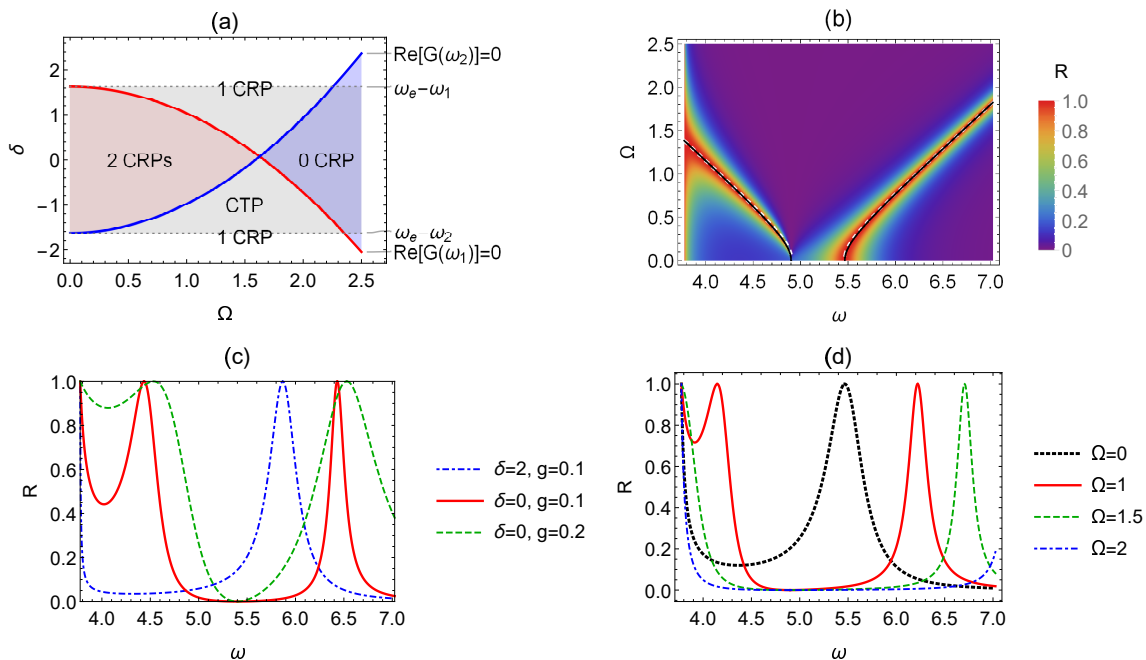


FIG. 2. (Color online) Single-mode regime analysis. (a) Phase diagrams of the number of complete reflection peaks (CRPs) and complete transmission peaks (CTPs) across varied driving field parameters Ω and δ ; (b) R as a function of ω and Ω , where black thick curves indicate complete reflection at $\text{Re}[G(\omega)] = 0$, and white dotted curves represent $\omega = \tilde{\nu}_{\pm}$; (c) Reflectance R versus ω for parameters $(\delta, g) = (2, 0.1), (0, 0.1), (0, 0.2)$ with $\Omega = 1$; (d) R plotted against ω for varying $\Omega = 0, 1, 1.5, 2$. In subfigures (b) and (d), $g = 0.1$ and $\delta = 0.5$. Additional parameters are $a = 1.5b$, cutoff frequencies $\omega_1 = 3.78$, $\omega_2 = 7.02$, and $\omega_e = (\omega_1 + \omega_2)/2$. Frequencies are normalized to c/b units.

IV. NUMERICAL ANALYSIS OF SINGLE-PHOTON TRANSPORT ACROSS SINGLE- AND MULTI-MODE REGIMES

This section numerically investigates how the driven Λ -type emitter precisely modulates single-photon transport in both single- and multi-mode regimes, and analyzes the dependence of this control on the incident photonic state.

A. Single-mode regime: precision tuning via the driven Λ -type emitter

Single-mode operation is defined by the spectral window $\omega_1 < \omega < \omega_2$ in which only the fundamental TM_{11} mode ($j = 1$) propagates. All frequencies are expressed in units of c/b , where c is the speed of light and b is the shorter transverse dimension of the rectangular waveguide. For $a = 1.5b$, the cut-offs are $\omega_1 = 3.78$ and $\omega_2 = 7.02$.

The emitter is initialized in the $|g\rangle$ and the incident photon in the single-photon state $|\varphi_{in}\rangle = |\varphi_{1,k_1}\rangle$ with frequency ω and longitudinal wave number $k_1 = \sqrt{\omega^2 - \omega_1^2}$. Restricting Eq. (17) to $j_{\max} = 1$ ($c_j = \delta_{j,1}$) gives the reflectance

$$R = 1 - T = \frac{\Gamma_1^2(\omega)}{|G(\omega)|^2}, \quad (25)$$

where $G(\omega) = \omega - \omega_e - \Omega^2/(\omega - \omega_e + \delta) - \Delta_1(\omega) + i\Gamma_1(\omega)$.

Single-mode EIT ($R = 0$) occurs at the incident photon frequency $\omega = \omega_e - \delta$. When the drive detuning δ lies within the interval $(\omega_e - \omega_1, \omega_e - \omega_2)$, the system exhibits a single CTP across the single-mode band. This phenomenon is vividly depicted by the gray-shaded region in Fig. 2(a), as well as by the solid red and dashed green curves in Fig. 2(c). Conversely, for δ outside this defined range, the condition of complete transparency is suppressed, as evidenced by the dot-dashed blue curve in Fig. 2(c).

Equation (25) specifies two scenarios for complete reflection. Firstly, when the photon frequency is in resonance with the cutoff, $\omega = \omega_1$, the group velocity $v_g = \rho_1^{-1}|_{\omega=\omega_1}$ becomes zero, which in turn gives rise to complete reflection. Secondly, the Fano resonance condition is satisfied when $\text{Re}[G(\omega)] = \omega - \omega_e - \Omega^2/(\omega - \omega_e + \delta) - \Delta_1(\omega) = 0$. Then the reflection spectrum is profoundly sensitive to the driving field. The number of CRPs is determined by the relative positions of the re-normalized transition frequencies $\tilde{\nu}_{\pm}$ with respect to the guided-mode band $[\omega_1, \omega_2]$, with Ω serving as the control parameter. As depicted in Fig. 2(d), three distinct regimes emerge. When both re-normalized frequencies lie within the guided-mode band $[\omega_1, \omega_2]$, two reflection channels are active, leading to the formation of two CRPs (represented by the solid red curve). If only one of the re-normalized frequencies falls within the guided-mode

band, a single reflection channel is present, resulting in a single CRP (the dashed green curve). When both re-normalized frequencies lie outside the guided-mode band, the system supports no reflection channels, and thus no CRPs are observed (the dot-dashed blue). These results are also confirmed by Figs. 2(a) and 2(b). The impact of the driving field is further clarified by examining the limit $\Omega \rightarrow 0$. In this case, the system's behavior reverts to that of a simple two-level emitter coupled to the waveguide. The condition for complete reflection simplifies to $\omega - \nu_- - \Delta(\omega) = 0$, which yields at most one CRP, as indicated by the dotted black curve in Fig. 2(d). Besides, the re-normalized transition frequencies $\tilde{\nu}_{\pm}$ in Eqs. (24a) and (24b) can also be explicitly tuned via the driving field's frequency detuning δ . And the emitter-waveguide coupling strength g governs the width of these spectral features. As g increases, the Lamb shift also increases, leading to a broadening of the reflection windows and a corresponding narrowing of the transmission windows. This effect is demonstrated by comparing the solid red and green dashed curves in Fig. 2(c).

In conclusion, we can achieve EIT-induced complete transmission by adjusting the δ , and control the re-normalized transition frequencies through parameters Ω or δ , thereby inducing Fano resonance for complete reflection.

B. Multi-mode regime: input state-dependent single-photon transport control

In this subsection, we extend our study of single-photon transport control from the single-mode to the multi-mode regime. Single-mode operation is confined to a narrow frequency range $\omega_1 < \omega < \omega_2$, yet practical applications often require operation at frequencies outside this range. When the photon frequency exceeds ω_2 , the waveguide naturally supports multiple transverse modes, with the number of active TM modes j_{\max} determined by the waveguide geometry and photon frequency via $\omega_{j_{\max}} < \omega < \omega_{j_{\max}+1}$. The multi-mode transition reveals two key phenomena: emitter-mediated inter-mode coupling and multi-path quantum interference. The constructive or destructive interference outcomes are determined by the relative amplitudes and phases of indistinguishable scattering paths. As the number of modes increases, these phenomena collectively dominate transport control. Eq. (17) indicates that the single-photon scattering in the multi-mode regime is modulated not only by the external drive through $G(\omega)$, but also by the incident state via expansion coefficients c_j .

Figure 3 presents reflection spectra for various input states in the multi-mode regime, focusing on two- and three-mode regimes under fixed drive parameters, revealing a pronounced input-state dependence. A single-mode state (SMS) injects the photon into one TM channel only, while a coherent superposition state (CSS) distributes it across multiple modes whose amplitudes in-

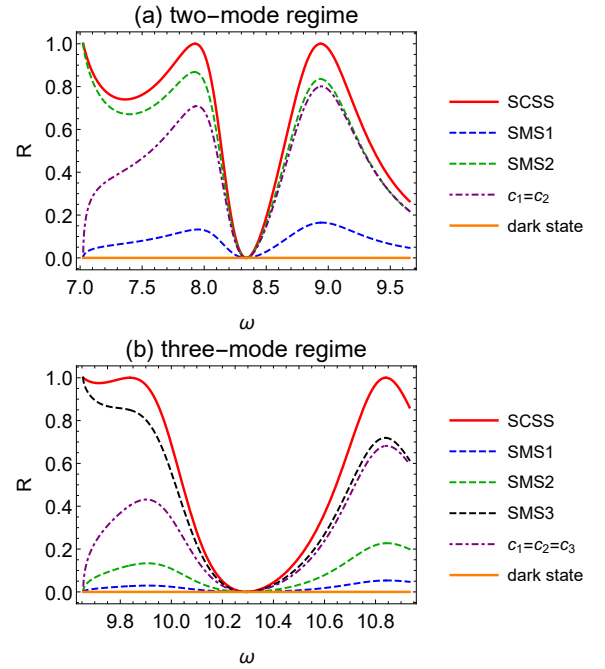


FIG. 3. (Color online) Reflectance $R(\omega)$ for various input states in (a) Two-mode and (b) three-mode regimes with $a = 1.5b$, $\Omega = 0.5$, $\delta = 0$, frequencies unitized as c/b . (a) Two-mode inputs: the specific coherent superposition state (SCSS, $c_j \propto \rho_j g_{j,k_j}^*$), the single-mode state in the TM_{11} mode (SMS1, $c_1 = 1, c_2 = 0$) and TM_{31} mode (SMS2, $c_1 = 0, c_2 = 1$), the equal-probability superposition state ($c_1 = c_2 = 1/\sqrt{2}$), and dark state ($\sum_{j=1}^{j_{\max}} c_j g_{j,k_j} = 0$), with $g = 0.1$, cutoffs $\omega_2 = 7.02$, $\omega_3 = 9.65$, $\omega_e = (\omega_2 + \omega_3)/2$. (b) Three-mode inputs: SCSS, SMS1, SMS2, the single-mode state in the TM_{13} mode (SMS3, $c_3 = 1, c_1 = c_2 = 0$), the equal-probability superposition state ($c_1 = c_2 = c_3 = 1/\sqrt{3}$), and dark state, with $g = 0.05$, cutoffs $\omega_3 = 9.65$, $\omega_4 = 10.93$, $\omega_e = (\omega_3 + \omega_4)/2$.

terfere through their common emitter interactions. For CSS, the scattering amplitude is not a weighted average of individual SMS results. An equal-probability CSS (purple dot-dashed) differs markedly from the arithmetic mean of the dashed SMS curves. Engineered interference within the CSS can cancel or enhance all forward waves, yielding unit reflection or transmission even when many channels are open—conditions unreachable by any SMS. The red solid curves, representing the specific coherent superposition state (SCSS, $c_j \propto \rho_j g_{j,k_j}^*$), reproduce the double-dip perfect reflection signature established in Sec. III; the orange solid curves (dark state, $\sum_j c_j g_{j,k_j} = 0$) show frequency-independent unit transmission; the dashed SMS curves exhibit only local Fano peaks and never reach $R = 1$. This comparison underscores the unique control power of CSS-mediated interference over quantum transport.

We now analyze how the driven Λ -type emitter controls single-photon scattering across the multi-mode frequency spectrum. We systematically compare two incident photon states: SCSS and SMS. For the SCSS we set

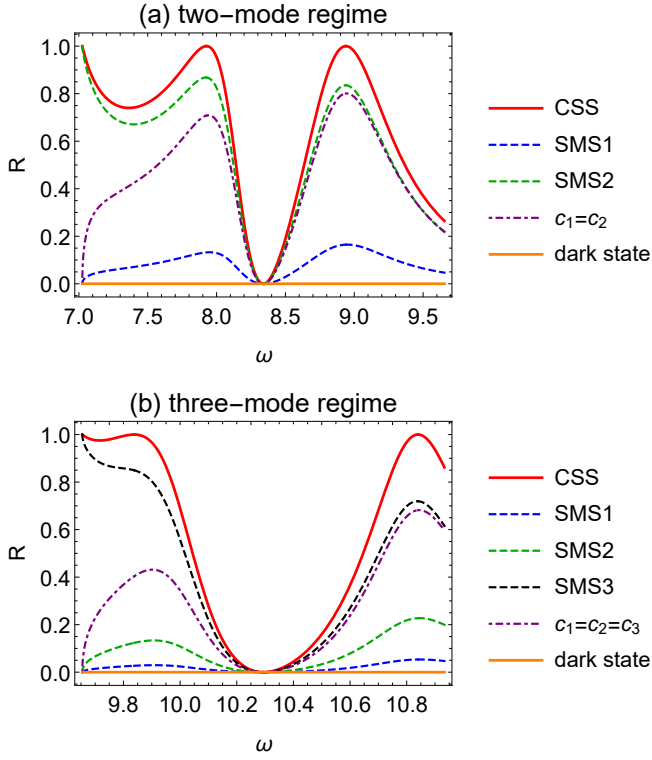


FIG. 4. (Color online) Two-mode regime analysis. (a-c) Total reflectance $R(\omega)$ with varying Ω and δ for input photon states: (a) the specific coherent superposition state (SCSS, $c_j \propto \rho_j g_{j,k_j}^*$), (b) the single-mode state in the TM_{11} mode (SMS1, $c_1 = 1, c_2 = 0$), and (c) the single-mode state in the TM_{31} mode (SMS2, $c_1 = 0, c_2 = 1$). (d-f) Mode-resolved reflectance ($R_i(\omega)$) and transmittance ($T_i(\omega)$) with $i = 1$ (TM_{11}) and $i = 2$ (TM_{31}) for (d) SCSS, (e) SMS1, and (f) SMS2, where $\Omega = 0.5$ and $\delta = 0$. Additional parameters: $a = 1.5b$, cutoffs $\omega_2 = 7.02$, $\omega_3 = 9.65$, $\omega_e = (\omega_2 + \omega_3)/2$, and $g = 0.1$. Frequencies are unitized as c/b .

$c_j \propto \rho_j g_{j,k_j}^*$ in Eqs. (16a)-(16b) to obtain the reflectance and transmittance of the j -th mode:

$$R_j = \frac{\Gamma_j(\omega)\Gamma(\omega)}{|G(\omega)|^2}, \quad (26a)$$

$$T_j = \frac{\Gamma_j(\omega)}{\Gamma(\omega)} - R_j. \quad (26b)$$

The total reflectance and transmittance are

$$R = 1 - T = \frac{\Gamma^2(\omega)}{|G(\omega)|^2}. \quad (27)$$

Comparison with Eq. (25) reveals that when the photon input state is a SCSS, its scattering characteristics resemble those observed in the single-mode frequency range. Fig. 4(a) shows the total reflectance $R(\omega)$ across the two-mode regime for varying driving field parameters Ω and δ . EIT-induced complete transmission, tuned by δ , produces a single CTP at $\omega = \omega_e - \delta$ (solid red and dashed green curves). Fano complete reflection, controlled jointly by Ω and δ , yields two CRPs

when $\text{Re}[G(\omega_{j_{\max}})] < 0 < \text{Re}[G(\omega_{j_{\max}+1})]$ (solid red curve). Additional control details are listed in Table I. Fig. 4(d) decomposes the reflectance and transmittance into their modal components to expose the underlying control. Multi-channel interference reduces the transmission amplitude of Eq. (15b) to $t_j = c_j[1 - i\Gamma(\omega)/G(\omega)]$, implying that a SCSS input is scattered identically in every TM_j mode. In each channel, the direct wave interferes with its scattered counterpart. The dashed green and dotted black curves in Fig. 4(d) show that Fano resonance drives the transmission amplitude of every mode to zero, giving complete reflection, while the solid red and dot-dashed blue curves show that EIT drives the reflection amplitude to zero, giving complete transmission.

For an input photon in the multi-mode frequency window prepared in the n -th single-mode state (SMS) $|\varphi_{in}\rangle = |\varphi_{n,k_n}\rangle$, inserting $c_j = \delta_{nj}$ into Eqs. (16a)-(16b) yields

$$R_n = \frac{\Gamma_n^2(\omega)}{|G(\omega)|^2}, \quad (28a)$$

$$T_n = |1 - \frac{i\Gamma_n(\omega)}{G(\omega)}|^2, \quad (28b)$$

$$R_j = T_j = \frac{\Gamma_n(\omega)\Gamma_j(\omega)}{|G(\omega)|^2} \quad (\text{for } j \neq n), \quad (28c)$$

with total reflectance and transmittance

$$R = 1 - T = \frac{\Gamma(\omega)\Gamma_n(\omega)}{|G(\omega)|^2}. \quad (29)$$

The emitter absorbs the n -th mode photon and decays into all available channels j at rates Γ_j . Figs. 4(b) and 4(c) present the resulting total reflectance in the two-mode regime for SMS1 (TM_{11}) and SMS2 (TM_{31}) inputs; Figs. 4(e) and 4(f) give the corresponding modal components. Inside the input channel ($j = n$), direct and scattered waves interfere partially. At Fano resonance, this interference drives the transmitted fraction to its minimum $T_{n,\min} = [\Gamma(\omega) - \Gamma_n(\omega)]^2/\Gamma^2(\omega)$ (dashed green curves in Figs. 4(e) and 4(f)), while boosting the reflection fraction to its maximum $R_{n,\max} = \Gamma_n^2(\omega)/\Gamma^2(\omega)$ (dot-dashed blue curve in Fig. 4(e), solid red curve in Fig. 4(f)). For non-input channels ($j \neq n$), symmetric coupling to left- and right-going waves yields equal reflectance and transmittance $R_j = T_j$ (solid red curve in Fig. 4(e) and dot-dashed blue curve in Fig. 4(f)), both peaking at the Fano frequency, $T_{j,\max} = R_{j,\max} = \Gamma_n(\omega)\Gamma_j(\omega)/\Gamma^2(\omega)$. Because $R_{\max} = \Gamma_n(\omega)/\Gamma(\omega) < 1$, SMS incidence never reaches unit reflectance, in contrast to the SCSS case. Moreover, only the highest-mode SMS can achieve $R = 1$ at its cutoff ($v_g = \rho_{j_{\max}}^{-1}|_{\omega=\omega_{j_{\max}}} = 0$) (Fig. 4(c)), whereas other SMS inputs transmit fully there (Fig. 4(b)). Nevertheless, complete transmission is recovered at the EIT point for the SMS case, mirroring the SCSS behaviour.

We conclude that the CSS-mediated interference governs the multi-mode single-photon transport, yielding

unit reflectance for the SCSS and unit transmittance for the dark state, whereas an SMS excitation is bounded by $\Gamma_n(\omega)/\Gamma(\omega) < 1$ reflectance and achieves $R = 1$ only when the SMS occupies the highest-mode channel at the corresponding cutoff frequency, while both classes recover perfect transmission at the EIT point.

V. DISCUSSION AND CONCLUSION

In this work, we have demonstrated the quantum control of single-photon scattering in both single- and multi-mode waveguide QED systems using the driven Λ -type emitter. The driven Λ -type emitter, with only one transition coupled to the waveguide, acts as a tunable V-type emitter whose two transitions are effectively coupled and whose two renormalized transition frequencies ν_{\pm} are continuously tunable via the driving-field detuning δ and Rabi frequency Ω . Using the Lippmann-Schwinger formalism, we derived the scattering matrix and identified key interference effects governing photon transport. Our results show that EIT enables complete transmission in both single- and multi-mode regimes by tuning δ , while Fano resonances dictate complete reflection—achievable in the single-mode regime when the photon frequency matches $\tilde{\nu}_{\pm}$. Notably, the number and position of these reflection peaks are fully controllable via δ and Ω , allowing precise spectral engineering. In the multi-mode regime, the input-photon states critically influences scattering. When the input is a specific coherent superposition (SCSS) with coefficients $c_j \propto \rho_j g_{j,k_j}^*$, multi-mode quantum interference reproduces single-mode-like behavior, restoring Fano-mediated complete reflection. In contrast, a single-mode photon (SMS) eliminates Fano effects, as the emitter only couples to the incident mode

while symmetrically scattering other modes, preventing complete reflection. Remarkably, complete transmission persists if the input state is a superposition of dark states, independent of the number of modes.

The tunability of multi-mode waveguides can be implemented in diverse platforms [9, 45–53], including optical fibers [47, 48], photonic crystal waveguides [49, 50], superconducting circuits [9, 51, 52], and Rydberg atom arrays [53], where multi-mode effects arise from modal dispersion or group-velocity splitting. A driven Λ -emitter can be realized in Josephson-junction-based fluxonium qubits [54, 55], quantum dots [56], or spin defects, ensuring broad applicability.

These findings advance the understanding of quantum interference in multi-mode waveguide QED and provide a versatile toolbox for photon manipulation. The ability to dynamically control reflection and transmission peaks enables the design of broadband frequency-selective filters, multi-mode spectrometers, and quantum routers, with direct implications for scalable quantum information processing. Future work may explore non-reciprocal scattering, multi-photon scattering, or many-body effects.

ACKNOWLEDGMENTS

Y. J. Song was supported by NSFC (No. 12205088). Y. Liu was supported by Scientific Research Fund of Hunan Provincial Education Department of China under Grant (No. 24C0353) and Key Laboratory of Opto-electronic Control and Detection Technology of University of Hunan Province under Grant (No. 2024HSKFJJ012). J. B. Yuan was supported by the Natural Science Foundation of Hunan Province under Grant (No. 2025JJ50005). S. Q. Tang was supported by Scientific Research Fund of Hunan Provincial Education Department of China under Grant (No. 22A0507).

-
- [1] X. Gu, A. F. Kockum, A. Miranowicz, Y. X. Liu, and F. Nori, Microwave photonics with superconducting quantum circuits, *Physics Reports* **718-719**, 1 (2017).
 - [2] A. González-Tudela, A. Reiserer, J. J. García-Ripoll, and F. J. García-Vidal, Light–matter interactions in quantum nanophotonic devices, *Nature Reviews Physics* **6**, 166 (2024).
 - [3] J.-T. Shen and S. Fan, Coherent single photon transport in a one-dimensional waveguide coupled with superconducting quantum bits, *Phys. Rev. Lett.* **95**, 213001 (2005).
 - [4] J.-T. Shen and S. Fan, Strongly correlated two-photon transport in a one-dimensional waveguide coupled to a two-level system, *Phys. Rev. Lett.* **98**, 153003 (2007).
 - [5] D. Roy, C. M. Wilson, and O. Firstenberg, Colloquium: Strongly interacting photons in one-dimensional continuum, *Rev. Mod. Phys.* **89**, 021001 (2017).
 - [6] H. J. Kimble, The quantum internet, *Nature* **453**, 1023–1030 (2008).
 - [7] L. Zhou, Z. R. Gong, Y.-x. Liu, C. P. Sun, and F. Nori, Controllable scattering of a single photon inside a one-dimensional resonator waveguide, *Phys. Rev. Lett.* **101**, 100501 (2008).
 - [8] L. Zhou, L.-P. Yang, Y. Li, and C. P. Sun, Quantum routing of single photons with a cyclic three-level system, *Phys. Rev. Lett.* **111**, 103604 (2013).
 - [9] B. Kannan, A. Almanakly, Y. Sung, A. D. Paolo, D. A. Rower, J. Braumüller, A. Melville, B. M. Niedzielski, A. Karamlou, K. Serniak, A. Vepsäläinen, M. E. Schwartz, J. L. Yoder, R. Winik, J. I.-J. Wang, T. P. Orlando, S. Gustavsson, J. A. Grover, and W. D. Oliver, On-demand directional microwave photon emission using waveguide quantum electrodynamics, *Nat. Phys.* **19**, 394 (2023).
 - [10] V. Paulisch, H. J. Kimble, and A. González-Tudela, Universal quantum computation in waveguide QED using decoherence free subspaces, *New Journal of Physics* **18**, 043041 (2016).
 - [11] L. García-Álvarez, J. Casanova, A. Mezzacapo, I. L. Egusquiza, L. Lamata, G. Romero, and E. Solano, Fermion-fermion scattering in quantum field theory with superconducting circuits, *Phys. Rev. Lett.* **114**, 070502 (2005).

- (2015).
- [12] T. Berndsen and I. M. Mirza, Electromagnetically induced transparency in many-emitter waveguide quantum electrodynamics: Linear versus nonlinear waveguide dispersions, *Phys. Rev. A* **108**, 063702 (2023).
- [13] U. Fano, Effects of configuration interaction on intensities and phase shifts, *Phys. Rev.* **124**, 1866 (1961).
- [14] Q. Li, L. Zhou, and C. P. Sun, Waveguide quantum electrodynamics: Controllable channel from quantum interference, *Phys. Rev. A* **89**, 063810 (2014).
- [15] S. Xu and S. Fan, Implications of exceptional points for few-photon transport in waveguide quantum electrodynamics, *Phys. Rev. A* **99**, 063806 (2019).
- [16] B. Kannan, M. J. Ruckriegel, D. L. Campbell, A. F. Kockum, J. Braumüller, D. K. Kim, M. Kjaergaard, P. Krantz, A. Melville, B. M. Niedzielski, A. Vepsäläinen, R. Winik, J. L. Yoder, F. Nori, T. P. Orlando, S. Gustavsson, and W. D. Oliver, Waveguide quantum electrodynamics with superconducting artificial giant atoms, *Nature* **583**, 775–779 (2020).
- [17] X.-J. Sun, W.-X. Liu, H. Chen, and H.-R. Li, Tunable single-photon nonreciprocal scattering and targeted router in a giant atom-waveguide system with chiral couplings, *Communications in Theoretical Physics* **75**, 035103 (2023).
- [18] X. Zhang, C. Liu, Z. Gong, and Z. Wang, Quantum interference and controllable magic cavity qed via a giant atom in a coupled resonator waveguide, *Phys. Rev. A* **108**, 013704 (2023).
- [19] J. X. Zhou, Z. H. Zhu, Y. Q. Zhang, K. K. Chen, Z. H. Peng, Y. F. Chai, Z. Z. Xiong, and L. Tan, Phase-modulated single-photon router and chiral scattering between two waveguides coupled by a giant three-level atom, *Laser Physics Letters* **21**, 055202 (2024).
- [20] G. Sun, Y. Yang, J. Li, J. Lu, and L. Zhou, Cavity-modified oscillating bound states with a Λ -type giant emitter in a linear waveguide, *Phys. Rev. A* **111**, 033701 (2025).
- [21] E. Kim, X. Zhang, V. S. Ferreira, J. Banker, J. K. Iverson, A. Sipahigil, M. Bello, A. González-Tudela, M. Mirhosseini, and O. Painter, Quantum electrodynamics in a topological waveguide, *Phys. Rev. X* **11**, 011015 (2021).
- [22] H. Zhu, X.-L. Yin, and J.-Q. Liao, Single-photon scattering in giant-atom topological-waveguide-qed systems, *Phys. Rev. A* **111**, 023711 (2025).
- [23] Y. Ashida, T. Yokota, A. m. c. İmamoğlu, and E. Demler, Nonperturbative waveguide quantum electrodynamics, *Phys. Rev. Res.* **4**, 023194 (2022).
- [24] Y. P. Peng and W. Z. Jia, Single-photon scattering from a chain of giant atoms coupled to a one-dimensional waveguide, *Phys. Rev. A* **108**, 043709 (2023).
- [25] W. Zhao, T. Tian, and Z. Wang, Single-photon scattering and bound states in a one-dimensional waveguide with a topological giant atom, *Phys. Rev. A* **109**, 063708 (2024).
- [26] W. Gu, H. Huang, Z. Yi, L. Chen, L. Sun, and H. Tan, Correlated two-photon scattering in a one-dimensional waveguide coupled to two- or three-level giant atoms, *Phys. Rev. A* **108**, 053718 (2023).
- [27] N. V. Corzo, J. Raskop, A. Chandra, A. S. Sheremet, B. Gouraud, and J. Laurat, Waveguide-coupled single collective excitation of atomic arrays, *Nature* **566**, 359–362 (2019).
- [28] E. Spiller and A. Segmüller, Propagation of x rays in waveguides, *Applied Physics Letters* **24**, 60 (1974).
- [29] K. Okamoto, T. Noma, A. Komoto, W. Kubo, M. Takahashi, A. Iida, and H. Miyata, X-ray waveguide mode in resonance with a periodic structure, *Phys. Rev. Lett.* **109**, 233907 (2012).
- [30] X.-C. Huang, T.-J. Li, F. A. Lima, and L.-F. Zhu, Classical, semiclassical, and quantum-optical models for an x-ray planar cavity with electronic resonance, *Phys. Rev. A* **109**, 033703 (2024).
- [31] J.-F. Huang, T. Shi, C. P. Sun, and F. Nori, Controlling single-photon transport in waveguides with finite cross section, *Phys. Rev. A* **88**, 013836 (2013).
- [32] H.-X. Song, X.-Q. Sun, J. Lu, and L. Zhou, Spatial dependent spontaneous emission of an atom in a semi-infinite waveguide of rectangular cross section, *Communications in Theoretical Physics* **69**, 59 (2018).
- [33] J. Zeng, Y. Song, J. Lu, and L. Zhou, Non-Markovianity of an atom in a semi-infinite rectangular waveguide, *Chinese Physics B* **32**, 030305 (2023).
- [34] Y.-J. Song, M.-Y. Chai, X.-W. Wang, J.-B. Yuan, S.-Q. Tang, and Y. Liu, Visualization of electromagnetic fields in a circular waveguide using Mathematica, *European Journal of Physics* **45**, 055202 (2024).
- [35] Y.-J. Song and L. Qiao, Controlling single-photon scattering in a rectangular waveguide by a V-type three-level emitter, *Optics Express* **28**, 37639 (2020).
- [36] J. Fu, Z. Si, S. Tang, and J. Deng, Classical simulation of quantum entanglement using optical transverse modes in multimode waveguides, *Phys. Rev. A* **70**, 042313 (2004).
- [37] X. Zhang, H. Li, R. Zeng, M. Hu, M. Xu, X. Zhou, Y. Lan, X. Xia, J. Xu, and Y. Yang, Nonreciprocal single-photon scattering mediated by a driven Λ -type three-level giant atom, *Communications in Theoretical Physics* **76**, 115501 (2024).
- [38] D. Witthaut and A. S. Sørensen, Photon scattering by a three-level emitter in a one-dimensional waveguide, *New Journal of Physics* **12**, 043052 (2010).
- [39] C. Martens, P. Longo, and K. Busch, Photon transport in one-dimensional systems coupled to three-level quantum impurities, *New Journal of Physics* **15**, 083019 (2013).
- [40] G. Yadav, M. M. Mahana, and T. N. Dey, Controllable single-photon scattering via coupling of a driven Λ system with a topological waveguide, *Phys. Rev. A* **112**, 023707 (2025).
- [41] D. Ilin and A. V. Poshakinskiy, Many-photon scattering and entangling in a waveguide with a Λ -type atom, *Phys. Rev. A* **109**, 033710 (2024).
- [42] M. P. Schneider, T. Sproll, C. Stawiarski, P. Schmitteckert, and K. Busch, Green’s-function formalism for waveguide qed applications, *Phys. Rev. A* **93**, 013828 (2016).
- [43] J. R. Taylor and H. Uberall, Scattering theory: The quantum theory of nonrelativistic collisions, *Physics Today* **26**, 55 (1973).
- [44] C. Cohen-Tannoudji, J. Dupont-Roc, G. Grynberg, and P. Meystre, Atom-photon interactions: basic processes and applications, *Physics Today* **45**, 115 (1992).
- [45] T. Levy-Yeyati, C. Vega, T. Ramos, and A. González-Tudela, Passive photonic cz gate with two-level emitters in chiral multimode waveguide qed, *PRX Quantum* **6**, 010342 (2025).
- [46] C. Vega, A. M. de las Heras, D. Porrás, and A. González-Tudela, Quantum state-controlled directional spontaneous emission of photons into a nanophotonic waveguide, *Quantum* **9**, 1861 (2025).

- [47] R. Mitsch, C. Sayrin, B. Albrecht, P. Schneeweiss, and A. Rauschenbeutel, Quantum state-controlled directional spontaneous emission of photons into a nanophotonic waveguide, *Nature Communications* **5**, 5713 (2014).
- [48] C. Sayrin, C. Junge, R. Mitsch, B. Albrecht, D. O’Shea, P. Schneeweiss, J. Volz, and A. Rauschenbeutel, Nanophotonic optical isolator controlled by the internal state of cold atoms, *Phys. Rev. X* **5**, 041036 (2015).
- [49] S. A. Skirlo, L. Lu, and M. Soljačić, Multimode one-way waveguides of large chern numbers, *Phys. Rev. Lett.* **113**, 113904 (2014).
- [50] S. Mahmoodian, K. Prindal-Nielsen, I. Söllner, S. Stobbe, and P. Lodahl, Engineering chiral light-matter interaction in photonic crystal waveguides with slow light, *Opt. Mater. Express* **7**, 43 (2017).
- [51] C. Joshi, F. Yang, and M. Mirhosseini, Resonance fluorescence of a chiral artificial atom, *Phys. Rev. X* **13**, 021039 (2023).
- [52] P. S. Shah, F. Yang, C. Joshi, and M. Mirhosseini, Stabilizing remote entanglement via waveguide dissipation, *PRX Quantum* **5**, 030346 (2024).
- [53] Y. Solomons and E. Shahmoon, Multichannel waveguide qed with atomic arrays in free space, *Phys. Rev. A* **107**, 033709 (2023).
- [54] N. Earnest, S. Chakram, Y. Lu, N. Irons, R. K. Naik, N. Leung, L. Ocola, D. A. Czapslewski, B. Baker, J. Lawrence, J. Koch, and D. I. Schuster, Realization of a Λ system with metastable states of a capacitively shunted fluxonium, *Phys. Rev. Lett.* **120**, 150504 (2018).
- [55] Y.-x. Liu, J. Q. You, L. F. Wei, C. P. Sun, and F. Nori, Optical selection rules and phase-dependent adiabatic state control in a superconducting quantum circuit, *Phys. Rev. Lett.* **95**, 087001 (2005).
- [56] H. Siampour, C. B. O’Rourke, A. J., M. N. Makhonin, R. Dost, D. J. Hallett, E. Clarke, P. K. Patil, M. S. Skolnick, and A. M. Fox, Observation of large spontaneous emission rate enhancement of quantum dots in a broken-symmetry slow-light waveguide, *npj Quantum Information* **9**, 15 (2023).